High-Resolution Model of Human Skin Appendages for Electromagnetic Dosimetry at Millimeter Waves

ZAIN HAIDER [1], **YVES LE DRÉAN** [2], **GIULIA SACCO** [1] **(Member, IEEE),**
DENYS NIKOLAYEV [1] **(Member, IEEE), RONAN SAULEAU** [1] **(Fellow, IEEE),**
AND MAXIM ZHADOBOV [1] **(Senior Member, IEEE)**

(Regular Paper)

[1]Univ Rennes, CNRS, IETR (Institut d'Électronique et des Technologies du numéRique), UMR 6164, F-35000 Rennes, France
[2]Univ Rennes, Inserm, EHESP, Institut de Recherche en Santé, Environnement et Travail (IRSET) - UMR_S 1085, F-35000 Rennes, France

CORRESPONDING AUTHOR: Zain Haider (e-mail: zain.haider@univ-rennes1.fr).

ABSTRACT The purpose of this work is to evaluate local power and electric field distributions inside high-resolution 3D anatomical CAD models of cutaneous appendages at 60 GHz upcoming for 5G/6G. The microscale resolution models of cutaneous nerves, lymphatics, pilosebaceous unit, microvasculature, eccrine sweat glands, Meissner corpuscle and Pacinian corpuscle were designed based on morphometric data and microscopic images. The Maxwell's and Hanai's mixture equations were employed to retrieve the complex permittivity of cutaneous appendages based on their free water content. The cutaneous appendages were exposed to a uniform plane wave. The finite element method was used to compute the power loss density (***PLD***) and internal electric field (***E***). The results indicate that the maximal ***PLD*** in cutaneous appendages occurred for ***E*** polarized along their longest dimension. Higher peak ***PLD*** was observed in high water content cutaneous appendages such as acrosyringium (45%), epidermal axon (37.9%), Pacinian corpuscle (32.5%), blood capillary (30.6%), lymph capillary (20%) and arrector pili muscle (13.5%) compared to the surrounding skin. Higher ***E*** was detected in low water content hair with the peak ***E*** 45.1% greater than in surrounding skin. The interfaces of the cutaneous appendages also manifested a boost (23.8%-60.9%) in ***PLD*** compared to the surrounding skin. Detailed physical interpretation of observed phenomena is provided in the article. These results provide an insight into microscale power deposition in skin at frequencies upcoming for wireless communications.

INDEX TERMS Dosimetry, finite element method, human skin, millimeter waves.

I. INTRODUCTION

In recent years, the prevalence of smartphones along with their data-intensive applications have spurred a phenomenal growth of mobile data traffic. According to the International Telecommunication Union (ITU), the exponential surge of mobile data traffic will reach 5 zettabyte/month by 2030 [1] whilst the number of devices connected to internet worldwide will exceed 75.4 billion by 2025 [2]. Evidently, the conventional microwave spectrum cannot serve this booming demand for higher data rates. Thus, the wireless industry is propelled towards underutilized millimeter wave (mmWave) bands. Since the launch of fifth generation (5G) mobile communications in the first quarter of 2020, mmWave spectra have been deployed to provide ultra-low latency ($\approx$1 ms) and ultra-high data rates

(several GB/s). The small cell infrastructure in the 5G era and beyond also targets to provide seamless coverage, ubiquitous connections and spectral efficiency. In particular, unlicensed allocations have been made in V-band for the development of 5G [3] and next generation Wi-Fi standard (e.g., WiGig) [4]. The mmWave spectrum is also critical for highly anticipated delay sensitive and high-speed communications such as virtual and augmented reality, IoT, autonomous vehicles, smart wearables, real-time telemedicine, remote surgery, and smart factory [2], [5], [6].

The systematic and continuous push towards the emerging 5G/6G mobile communications will make human exposure to mmWave radiation ubiquitous worldwide. As a consequence, development of tissue models accounting for local power deposition in cutaneous layers has become paramount for accurate dosimetry at these frequencies.

The anthropomorphic computational models (Virtual Family, Visible Human, etc.) have yielded a wealth of scientific knowledge on microwave dosimetry [7], [8]. However, the millimeter resolution of the voxel-based models is not enough to resolve skin substructures [9]. Early investigators resorted to theoretical calculations to evaluate power absorption within homogeneous [10] and planar stratified semi-infinite models [11] of human skin. For body-centric antenna and propagation measurements generic homogeneous skin-equivalent semi-solid [12] and solid [13] models were also introduced.

Human skin is neither homogeneous nor isotropic, rather it is a highly complex heterogeneous structure. Alekseev and Ziskin pioneered the numerical investigation of selective absorption of mmWave energy by cutaneous blood vessels, hair and sweat ducts as the complex permittivity of such skin appendages differ appreciably from the mean value for human skin [14], [15]. Their finite-difference-time-domain (FDTD) analysis at 42.25 GHz revealed that the specific absorption rate (SAR) inside the cutaneous blood vessels is substantially higher ($\approx$40%) than that of dermis and is a function of orientation of the incident electromagnetic (EM) field. Two-dimensional (2D) models of sweat duct and hair are considered in their work. Horizontal plexus of cutaneous blood vessels is modeled in three dimensions (3D) without taking into account the associated capillary loops. Another step towards understanding the interaction of mmWave with human skin was spearheaded by Feldman *et al.*, who promulgated the hypothesis that helical portion of the sweat duct in epidermis might act as an array of low Q helical antennas between 200 and 450 GHz [16]–[18]. Although significant progress has been made in the field of skin dosimetry at mmWaves, understanding of the power deposition in cutaneous layers at micro-scale level requires additional investigation.

In this paper, we report high-resolution 3D models of a complete set of human skin sub-structures (blood vessels, nerve fibers, lymphatic vessels, eccrine sweat glands, sebaceous glands, hair, arrector pili muscle, Pacinian corpuscle, and Meissner corpuscle) developed based on anatomical data. These models are used for the first-time for local micro-scale resolution dosimetry at 60 GHz to quantitatively analyze the electric field (E) and power loss density (PLD) distributions in the skin sub-structures. Different polarizations are considered to resolve finer details and analyze hot-spot formation.

II. MATERIALS AND METHODS
A. GEOMETRIC MODEL OF INTEGUMENTARY SYSTEM
Skin model consisted of three distinct layers: stratum corneum, epidermis and dermis with a typical thickness of 11 μm, 120 μm and 1.1 mm, respectively. The thickness of stratum corneum, epidermis and dermis in general vary between 8.08–13.66 μm, 31.2–189.2 μm and 0.46–1.9 mm, respectively [19], [20]. A 3D sinusoidal surface (1) was used to model the height (h) of the junction between epidermis and dermis [Fig. 1(h)]:

$$h = \pm A \cos\left(\frac{2\pi x}{S}\right) \cos\left(\frac{2\pi y}{S}\right) \qquad (1)$$

where, S = 0.21 mm and A = 30 μm are span and amplitude, respectively. The distribution density of dermal papillae was $\approx$40 per 1 mm^2 [21].

1) CUTANEOUS INNERVATION
The skin contains a dense network of nerve fibers as shown in Fig 1(a) [22]. The horizontally arranged small nerve bundles in the subepidermal neural plexus were represented by a cylinder with a typical diameter and length of 10 μm [23] and 0.2 mm, respectively [Fig. 1(a)]. The length of the superficial neural plexus in general varies between 42–100 mm per mm^2 [24]. The plexus was positioned at a typical depth of 0.2 mm from the skin surface. However, it can be as close as 0.1 mm from the surface of the skin [25]. Three C-fibers with a typical diameter of 1.5 μm and one $A\delta$ fiber with a diameter of 3 μm arborized from plexus at a distance of 25 μm [26] from dermo-epidermal junction and meandered towards vital layers of epidermis [Fig. 1(a)]. The variation of diameter of $A\delta$ fibers is generally between 1–6 μm whereas the diameter of C-fibers can be as low as 0.2 μm [27]. Moreover, the spatial density of epidermal nerve fibers in general varies between 0.5–8.5 per 0.01 mm^2 [24], [28]. The depth of intraepidermal nerve fibers from stratum corneum was selected to be 0.4 μm [29] and 4.75 μm, respectively.

2) CUTANEOUS LYMPHATICS
The cutaneous lymphatic network originates in the dermal papillae as blind ended tubes which drain into two horizontally running channels [Fig. 1(b)] [30]. The diameter of the lumen of lymphatic capillary was 25 μm. However, it can be as low as 15 μm [31]. The diameter of vessels in superficial and deep plexus was 50 μm and 100 μm, respectively. The variation in diameter of superficial and deep plexus is in general between 50–100 μm [32]. The lymphatic capillary was located at a depth of 50 μm from dermo-epidermal junction [33]. However, it can be as close as 25 μm from the junction [33]. The superficial plexus was located at a depth of 280 μm from the dermo-epidermal junction whereas deep lymphatic plexus
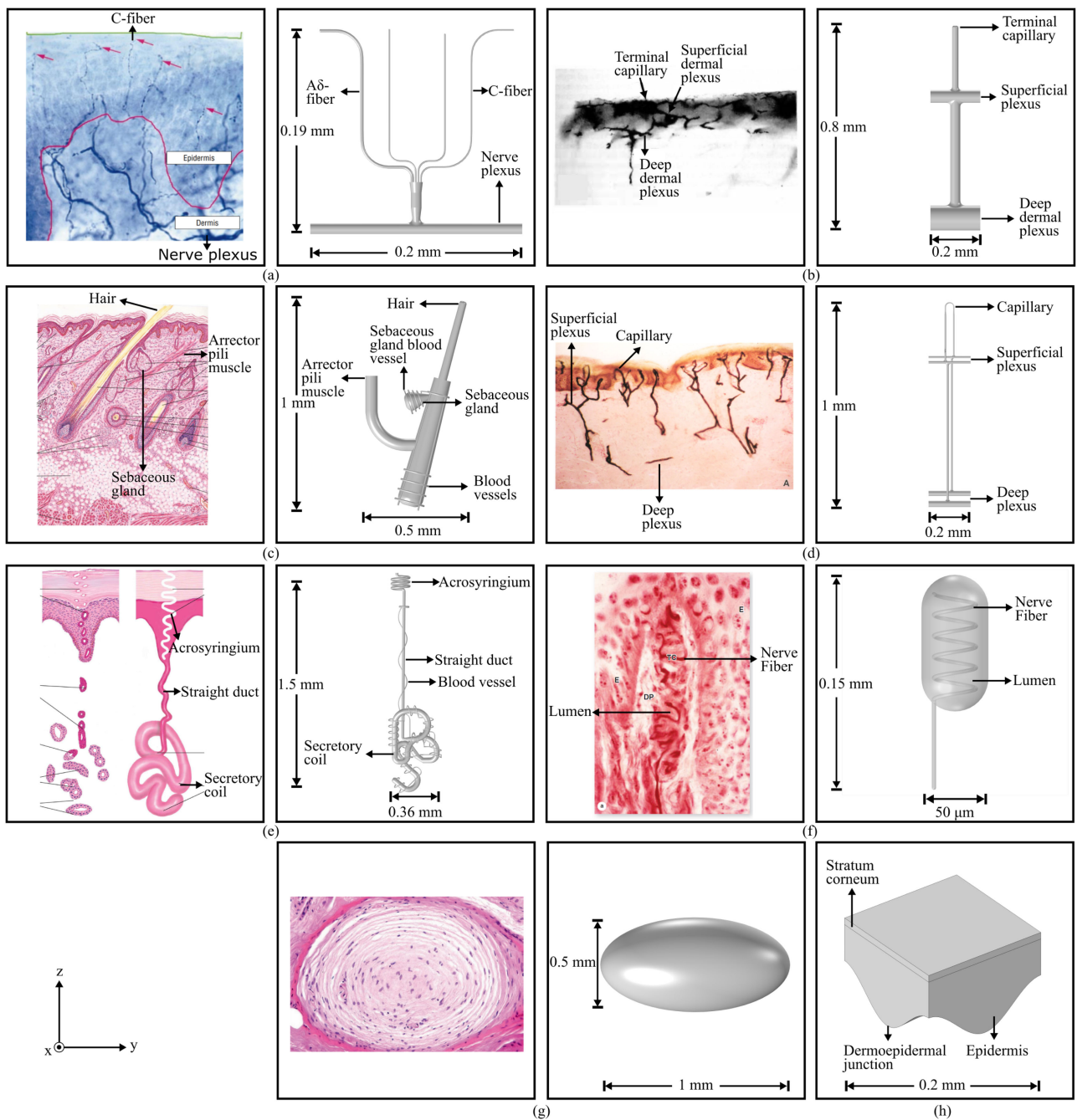
FIGURE 1. Geometric model: (a) cutaneous nerves microscopic image [22] and 3D model; (b) cutaneous lymphatic microscopic image [30] and 3D model; (c) pilosebaceous unit microscopic image [36] and 3D model; (d) cutaneous microvasculature microscopic image [48] and 3D model; (e) eccrine sweat gland microscopic image [36] and 3D model; (f) Meissner corpuscle microscopic image [57] and 3D model; (g) Pacinian corpuscle microscopic image [59] and 3D model; (h) Stratum corneum and epidermis 3D model. Reprinted with the permissions from Elsevier.

was located at a depth of approximately 900 µm from the skin surface. The depth of the superficial plexus from the dermo-epidermal junction generally varies between 50–300 µm [34]. Moreover, the vertical length of the lymphatic capillary was 0.245 mm whereas the horizontal length of lymphatic vessels was 0.2 mm [30]. Lastly, the mean lymphatic vessel density in papillary and reticular dermis was 18.1±5.3 per mm^2 and 8.9±1.2 per mm^2, respectively [35].

3) PILOSEBACEOUS UNITS

The pilosebaceous unit comprised of hair follicle, hair, sebaceous gland and arrector pili muscle as displayed in Fig. 1(c) [36]. The vellus hair follicle was represented by a cone with a typical top diameter of 86 µm and a length of 0.64 mm [37]. The density of hair follicles at different body sites varies between 0.14 and 2.92 per mm^2 [38]. The portion of hair anchored in hair follicle was roughly 0.6 mm

long while the portion of the hair emerging out of skin was about 0.3 mm in length. The top and bottom diameter of hair cone were approximately 36 μm and 54 μm. The variation of diameter of the hair is generally between 16–80 μm [39], [40]. The hair protruded from the skin at an angle of 30° [41].

The arrector pili muscle associated with hair follicle was modeled by a meandered cylinder with a typical diameter of 60 μm that spanned between epidermis and hair follicle. The diameter of arrector pili muscle generally varies between 10–140 μm [42]. It was connected to hair follicle at a depth of roughly 0.4 mm and had a total length of about 0.54 mm.

The sebaceous glands were saccular and ovoid with a typical diameter and length of 120 μm and 125 μm, respectively [43], [44]. The sebaceous glands were linked to the lumen of hair follicle via a small duct at a depth of roughly 0.16 mm [45]. In most parts of human skin, the density of sebaceous glands is less than 1 per mm² [44]. Lastly, microscopy data issued from [46], [47] were used to model the capillaries of hair follicle and sebaceous glands as shown in Fig. 1(c).

4) CUTANEOUS MICROVASCULATURE

The cutaneous microvasculature was organized into two main interconnected networks of blood vessels as shown in Fig. 1(d) [48]. The lumen of arteries and veins of the superficial plexus were modeled with cylinders with a typical diameter of 10 μm and 12.5 μm and were located at a typical depth of 0.35 mm from the skin surface. The diameter of the lumen of arteries and veins in the superficial plexus generally varies between 7.5–12 μm and 10–15 μm [49]. The range of variation of the depth of superficial plexus from the skin surface is 0.2–0.4 mm [14], [50]. The length of the vessels was fixed at 0.2 mm.

The arterial limb, venous limb and the intrapapillary loop that constituted the endothelial tube of the capillary had a typical diameter of 6.25 μm, 8 μm and 4.25 μm, respectively. The diameter of the endothelial tube of the arterial limb, venous limb and intrapapillary loop in general varies between 5–7.5 μm, 6–10 μm and 3.5–6 μm, respectively [49]. The length and width of the capillary loop was about 250 μm and 45 μm. Generally, the length and width of the capillary loop varies between 23.3–270 μm and 32–46.1 μm [51]. The number of capillary loops varies from 20–150 per mm², which in average corresponded to one capillary loop per 0.04 mm² [52].

The lumens of arteries and veins of the deep dermal plexus were also modeled with cylinders with a typical diameter of 25 μm and 30 μm. The outside diameter of vessels in deep dermal plexus in general varies between 40–50 μm [48]. The deep dermal plexus was positioned at a depth of 1 mm from the skin surface [53]. However, the deep plexus can be as deep as 1.5 mm from the skin surface [53]. Two vertical tributaries connected the upper plexus to lower one. The depth dependent distribution of cutaneous blood vessels was used to model arterioles and venules (2 per mm²) [54].

5) ECCRINE SWEAT GLANDS

Eccrine sweat glands are widely distributed in skin (0.13-3.6 per mm²) [47], [55]. It was composed of an excretory duct and a secretory portion [36] (Fig. 1(e)). The inner typical diameter of the convoluted secretory duct embedded deep into dermis was set to 40 μm. However, the diameter of the lumen of the secretory duct can be as low as 30 μm [56]. Moreover, the overall diameter of the secretory portion was roughly fixed at 600 μm. The variation of overall diameter of the secretory portion is in general between 500–700 μm. The total length and inner diameter of the straight excretory duct emerging from the secretory portion were roughly 1 mm and 20 μm. The length of straight duct can be up to 2 mm whereas the diameter of its lumen can be as low as 10 μm [56]. The distal helical segment (acrosyringium) of the excretory duct consisted of three turns whereas the axial pitch, major and minor radius of the helix were 60 μm, 120 μm and 20 μm, respectively. The minor radius of the helix can be up to 60 μm [56]. Lastly, in the absence of the quantitative data regarding blood supply, microscopy images [47] were used to sketch the capillaries (diameter = 6.5 μm) [49] wrapped around the secretory portion. One of the capillaries from the secretory portion also spiraled along the straight duct.

6) MEISSNER CORPUSCLES

Meissner corpuscle was modeled by a tapered cylindrical structure with the typical dimensions of $50\ \mu m \times 100\ \mu m$. The width and length of Meissner corpuscle can vary between 30–75 μm and 50–150 μm, respectively [57] [Fig. 1(f)]. The diameter of the spiraling nerve fiber associated with Meissner corpuscle was about 3 μm. They were localized between epidermal ridges at a depth of roughly 0.1 mm from the skin surface and are numerous within skin (20–50 per mm²) [58].

7) PACINIAN CORPUSCLES

An ellipsoid with the typical dimensions of 1 mm × 0.5 mm × 0.5 mm was used to model Pacinian corpuscle [59] [Fig. 1(g)]. The dimensions of the Pacinian corpuscle can be as large as 2.5 mm × 0.75 mm [60]. It was located roughly at a depth of 1 mm from the skin surface. The distribution density of the Pacinian corpuscles was reported to be 5–10/cm² [61].

B. ELECTROMAGNETIC PROPERTIES

The complex permittivity of stratum corneum [62], epidermis and dermis [62], blood [63], arrector pili muscle [63] and hair [15] at 60 GHz are summarized in Table 1. Owing to lack of experimental data on the electromagnetic properties of rest of the skin appendages, the mixture equations were employed to derive the complex permittivity based on their distinctive water content. The complex permittivity of pure water at skin temperature (33 °C) [64] was evaluated by using Ellison model [65]. The permittivity (≈2.5) of proteins [62] was used to model the volume fraction of dry components.

TABLE 1. Water Content and Complex Permittivity at 60 GHz

Compartment	Water Content	Bound Water	Complex Permittivity
Stratum corneum [62]	–	–	3.5-0.51j
Epidermis and Dermis [62]	–	–	8.17-11.27j
Blood [63]	–	–	12.3-16.4j
Arrector pili muscle [63]	–	–	12.9-15.8j
Hair [15]	–	–	2.6-0.1j
Water [65]	–	–	15.2-23.3j
Lymph [67]	96.6%	1.1%	14.84-22.3j
Axoplasm [68]	84.74%	4.9%	13.04-18.46j
Remak bundles [73]	71.56%	9.13%	11.2-14.5j
Sweat [69]	97.79%	0.7%	15.02-22.7j
Sebaceous glands [70]	13.2%	22.5%	4.4-1.7j
Humid Hair [71]	0.1%	32.1%	3.34-0.3j
Pacinian corpuscle [60]	91.1%	2.86%	13.99-20.51j
Meissner corpuscle lumen [73]	70.8%	9.4%	11.1-14.2j

1) WATER

The mass fraction of the biomolecules and water in various skin appendages was converted to the volume fraction by using a mass density of 1.35 g/cm^3 [66] and 1 g/cm^3, respectively (Table 1). The selected values for axoplasm (Squid giant axon) are close to the data reported for small axons (90-91%) [72]. Moreover, since the major portion of Meissner corpuscle's lumen and Remak bundles is occupied by Schwann cells, the water content of Schwann cells ($\approx$75%) [73] was used as a first approximation.

2) BOUND WATER

In this work, 0.35 g (0.2-0.65 g) of bound water per g of biomolecules was assumed to evaluate the volume fraction of water bound to polar groups and charged sites on the surface of biomolecules [74], [75] (Table 1).

3) MIXTURE MODEL

The mixture equations were applied in two steps. First, the Maxwell's mixture equation (2) [76] was used to enumerate the effective complex permittivity of hydrated biomolecules (ε_e^*).

$$\frac{\varepsilon_e^* - \varepsilon_b^*}{\varepsilon_e^* + \varepsilon_b^*} = p\frac{\varepsilon_p^* - \varepsilon_b^*}{\varepsilon_p^* - 2\varepsilon_b^*} \tag{2}$$

where p is the volume fraction taken by the biomolecule, ε_p^* and ε_b^* are the complex permittivity of the biomolecule and bound water shell, respectively. Since, the Maxwell's mixture equation only gives best accuracy for dilute suspensions

($p\approx$30%) [74], in the second step Hanai's mixture equation (valid up to ϕ=0.8) [77], [78] was utilized to extract the complex permittivity of the skin appendages (ε^*):

$$1 - \phi = \frac{\varepsilon^* - \varepsilon_e^*}{\varepsilon_w^* - \varepsilon_e^*}\left(\frac{\varepsilon_w^*}{\varepsilon^*}\right)^{1/3} \tag{3}$$

where ϕ is the volume fraction occupied by the hydrated biomolecules and ε_w^* is the complex permittivity of the free water molecules.

C. NUMERICAL METHOD

The full-wave electromagnetic simulations were performed using finite element method implemented in COMSOL Multiphysics (RF module). The source was a TE and TM plane wave (10 W/m^2 at 60 GHz). The periodic boundary conditions (Floquet periodicity) were applied in the x and y directions to simulate an infinite structure. A free space padding of 0.25 mm was inserted between the periodic port and the skin model (in case of the hair follicle, a padding of 0.35 mm was added). The outgoing waves were absorbed by 8-layered perfectly matched layer. The computational volume (0.2 mm $\times$ 0.2 mm $\times$ 1.1 mm) in majority of simulations was discretized into roughly 3×10^6-5×10^6 tetrahedral Lagrange quadratic mesh elements. The minimum and maximum mesh cell size was within 0.05–30 µm range. The numerical simulations were performed on a high-performance work station equipped with 36-core dual CPU of Intel Xeon(R) Gold 6140 (2.3–3.7 GHz) with 768 GB RAM. This numerical approach was validated on canonical analytical model in our previous study [79]. Lastly, the numerical simulations were performed on isolated skin appendages since simulating a complete skin model containing all skin appendages would require computational resources exceeding the capabilities of the high-performance workstations used in this study.

D. DOSIMETRY METRICS

PLD was used to assess the local power loss per unit volume in the skin substructures ($PLD = \frac{1}{2}\sigma_e|E|^2$ where $\sigma_e = \sigma_s + \omega\epsilon''$). The maximum electric field (E_{max}) and maximum power loss density (PLD_{max}) represent the highest values of E and *PLD* in the skin appendages. For comparison, the E_{max} and PLD_{max} were then normalized with respect to E and *PLD* in the surrounding skin (defined as the uniform E and *PLD* in skin sufficiently far from the local distortions created by skin appendages and located at the same depth). Note that, although skin at microscale level is comprised of individual cells, recent microdosimetry study at the level of single skin cell model revealed that *PLD* distribution within cellular compartments is nearly uniform at 60 GHz [84]. Lastly, average electric field (E_{avg}) and average power loss density (PLD_{avg}) were evaluated as E and *PLD* averaged over the volume of skin substructure.

III. RESULTS

Table 2 summarizes the E_{max} and PLD_{max} in various skin appendages compared to surrounding skin and skin surface. In

TABLE 2. Local Dosimetry Metrics Within Skin Appendages at Typical Depths for Incident Power Density of 10 W/m^2

Skin appendages	Compared to background skin		Compared to skin surface		Maximal values		Mean values	
	E_{max}	PLD_{max}	E_{max}	PLD_{max}	E_{max} (V/m)	PLD_{max} (kW/m³)	E_{avg} (V/m)	PLD_{avg} (kW/m³)
Acrosyringium	↘ 5%	↗ 45%	↘ 9%	↗ 97.2%	34.6	45.2	26.6	27.5
Axoplasm	↘ 0.8%	↗ 37.9%	↘ 2.8%	↗ 97.1%	37.1	42.5	27.4	23.7
Pacinian corpuscle	↘ 9.66%	↗ 32.5%	↘ 88.2%	↘ 44.1%	4.53	0.69	2.6	0.25
Blood capillary	↘ 0.5%	↗ 30.6%	↘ 18.1%	↗ 95.4%	31.4	26.9	19.5	10.7
Meissner corpuscle's axon	↘ 10.4%	↗ 23.9%	↘ 31.2%	↗ 94.2%	26.2	21.2	23.1	16.5
Lymphatic capillary	↘ 20.7%	↗ 20%	↘ 39.2%	↗ 93.8%	23.3	20.2	15.8	9.5
Arrector pili muscle	↘ 9.2%	↗ 13.5%	↘ 24%	↗ 94%	29.1	22.3	17.5	8.6
Sebaceous gland	↗ 36.96%	↘ 61.8%	↘ 4.02%	↗ 67.6%	36.8	3.9	30.4	2.6
Hair	↗ 45.05%	↘ 97.1%	↗ 41.6%	↘ 43.04%	65.7	0.71	33	0.2

*↘ and ↗ denote decrease and increase, respectively, compared to background skin or skin surface.
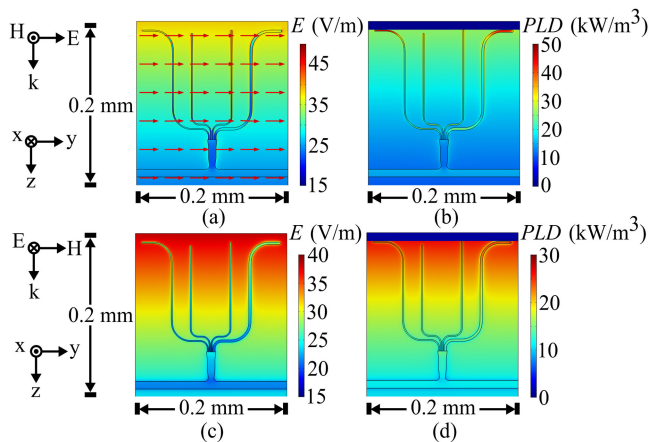

FIGURE 2. Cutaneous nerves: (a), (c) *E* (arrows in the figure only show the *E* field direction and not the amplitude); (b), (d) *PLD* distribution.

addition, E_{avg} and PLD_{avg} within different skin appendages is also presented. Note that the data in Table 2 correspond to the polarization (TE or TM) resulting in PLD_{max} within the skin appendages.

A. NERVES

Fig. 2 illustrates E and PLD distributions in cutaneous nerves. The maximum PLD (42.5 kW/m³) in the horizontal segment of the epidermal axoplasm when incident E was oriented parallel to it was roughly 37.9% higher than in the surrounding skin [Fig. 2(b)]. This local enhancement in PLD was primarily due to the higher conductivity of axoplasm as the induced E (37.1 V/m) inside the horizontal axoplasm approached the incident E (37.4 V/m) at axoplasm/epidermal interface due to continuity of the tangential components of E [Fig. 2(a)]. Contrarily, in case of orientation of E normal to the lateral surface of the axoplasm, the maximum PLD (24 kW/m³) inside the axoplasm was about 7.4% lower than in the surrounding skin [Fig. 2(d)]. This was in accordance with boundary conditions

on normal E at axoplasm/skin interface, which required a reduction in the internal E (27.9 V/m) relative to the incident E (37.1 V/m) by a factor of roughly the relative permittivity of axoplasm [Fig. 2(c)]. It is worthwhile to mention that the maximum PLD inside the axoplasm was 97.1% higher than at the surface of stratum corneum for the former polarization. On the contrary, the peak E (37.1 V/m) in the axoplasm was 2.8% lower than at the skin surface for the polarization shown in Fig. 2(a).

For E perpendicular to the vertical section of the axoplasm, the maximal PLD (40.05 kW/m³) and E (46.1 V/m) localized at axoplasm/skin interface was up to 35.1% and 37.1% higher than maximal PLD and E induced inside axoplasm for both polarizations [Fig. 2(a, b)]. This was the direct consequence of the Gauss's law ($\varepsilon_1 E_1^\perp - \varepsilon_2 E_2^\perp = \rho_s$), which led to accumulation of surface charges at the dielectric discontinuities. Although the thicker $A\delta$ fiber produced greater distortions in E and PLD than thinner C-fiber, the average E and PLD in $A\delta$ and C-fiber differed by less than 1%. This suggests that power loss inside various nerve fibers in skin is almost independent of their diameter. Moreover, for both polarizations, E (29 $\Rightarrow$ 22 V/m) and the corresponding PLD (27 $\Rightarrow$ 15 kW/m³) decreased monotonically by 24.1% and 44.4% in the straight section of the central axoplasm (100 μm long). The E and PLD inside the skin model at the same depth was 24.1% and 6.25% higher than that of the axoplasm for both polarizations. The swifter decay of E in axoplasm was due to its higher permittivity and conductivity compared to the background skin.

Lastly, the peak PLD (15.09 kW/m³) in horizontal plexus was also 22.3% higher than in the surrounding skin for E parallel to its longest dimension [Fig. 2(b)]. In contrast, for E polarized normal to the lateral surface of the plexus, the peak PLD (11.3 kW/m³) in the plexus was 6.9% lower than that in the surrounding skin [Fig. 2(d)]. The relatively lower increase in plexus in comparison to epidermal axons was mainly due to lower conductivity of Remak bundles. It is worthwhile to
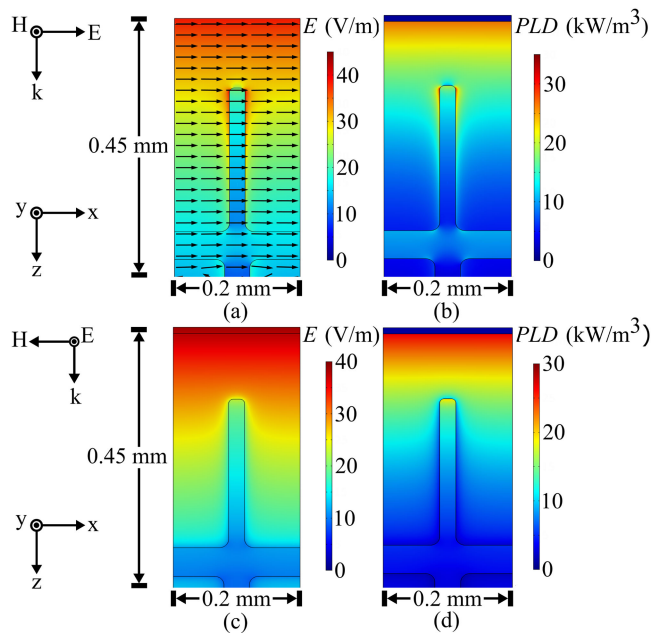
FIGURE 3. Cutaneous lymphatic: (a), (c) *E* distribution; (b), (d) *PLD* distribution.

FIGURE 4. Pilosebaceous unit: (a), (c) *E* distribution; (b), (d) *PLD* distribution.

mention that both *E* and *PLD* in the cross sections of nerves transverse to the propagation direction were uniform as the dimensions of nerves were an insignificant fraction of wavelength (0.003λ) in skin at 60 GHz.

B. LYMPH

Fig. 3 displays *E* and *PLD* in the longitudinal cross section of cutaneous lymphatic vessels in papillary dermis. The maxima of the *PLD* (20.2 kW/m^3) in the terminal portion of the open-ended lymphatic capillary were 20% higher than undistorted *PLD* in surrounding skin for the polarizations shown in Fig. 3 (b, d), respectively. The *E* in the capillary (23.3 V/m) was 20.7% weaker than the surrounding skin as *E* was normal to lateral surface of the capillary for both polarizations. Notice that the peak *PLD* in the lymphatic capillary was 93.8% higher than at the skin surface whereas maximal *E* was 39.2% lower.

Conversely, for *E* polarized along the axis of the horizontal plexuses located in papillary and reticular dermis, *PLD* in superficial (9.75 kW/m^3) and deep plexus (1.1 kW/m^3) was 51.5% and 51.8% higher than in surrounding skin [Fig. 3(b)]. The corresponding *E* in the superficial (16.2 V/m) and deep plexus (5.5 V/m) was almost similar (difference $= 2\%$) to the surrounding skin due to the continuity of the tangential component of *E*. Moreover, for the polarization shown in Fig. 3(d), *PLD* in superficial (4.36 kW/m^3) and deep dermal plexus (0.54 kW/m^3) was 11.5% and 13.5% lower than that in surrounding skin. This is due to 33.1% and 33.9% weak *E* in superficial (10.8 V/m) and deep plexus (3.8 V/m) from surrounding skin as *E* was normal to the vessels. Note that *E* was 0.8% weaker in the thicker vessels. The aforementioned results suggest only a marginal effect of vessel diameter on induced *E*.
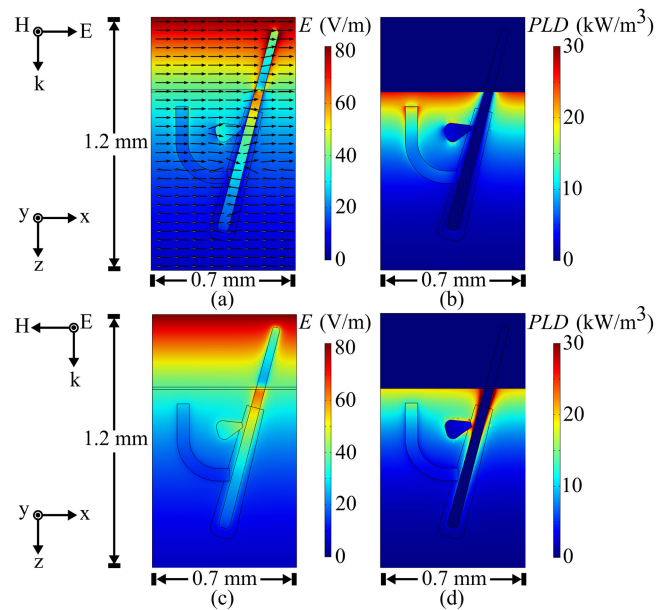
For polarizations in Fig. 3(b, d), the exponential decay of *PLD* from the capillary (20.2 kW/m^3) to the distal end of lymphatic vessel (0.8 kW/m^3, 0.6 kW/m^3) was 96%-97%. The monotonous decay in corresponding *E* from capillary (23.3 V/m) to posterior end (4.6 V/m, 4.03 V/m) of the lymph vessel was 80.2%-82.7%. Notice that the peak *E* (40 V/m) and *PLD* (31 kW/m^3) at the interface of the terminal capillary with skin were 29% and 50% higher than in surrounding skin [Fig. 3(a, b)]. Lastly, since the diameter of lymphatic vessels was much smaller than the wavelength ($\lambda/20$), *E* and *PLD* inside the lymphatic vessels were almost uniform in the *E-H* plane.

C. PILOSEBACEOUS UNIT

The details of local *E* and *PLD* through a central plane of pilosebaceous unit are shown in Fig. 4. The analysis of Fig. 4(a, c) revealed that the peak *E* was not located at the outer boundary of hair or skin. Rather, the site of maximal *E* (62.9 V/m-65.7 V/m) was inside the portion of hair that was embedded in epidermis. This can be attributed to low permittivity and conductivity of hair due to its lower water content. The maximum induced *E* inside the hair (65.7 V/m) and sebaceous gland (36.8 V/m) was 45.05% and 36.96% higher than surrounding skin for the orientation of *E* perpendicular to the base of the sebaceous gland [Fig. 4(a)]. Contrarily, for the polarization of *E* parallel to the base of the sebaceous gland, the peak *E* in hair (62.9 V/m) and sebaceous gland (29.4 V/m) was 40.5% and 15.7% higher than in surrounding skin [Fig. 4(b)]. Note that for both polarizations the peak *E* in hair was 39.2%-41.6% higher than at the skin surface whereas the peak *E* in the sebaceous glands was 4.02% and 22.9% lower for the polarization shown in Fig. 4(a, c), respectively.

Despite the high levels of E, the corresponding PLD in hair (0.71 kW/m^3) and sebaceous gland (3.9 kW/m^3) was roughly 97.1% and 61.8% lower compared to the surrounding skin for the former polarization whereas for the latter one PLD in hair (0.65 kW/m^3) and sebaceous gland (0.25 kW/m^3) was 97.5% and 78.7% lower. It is worthwhile to mention that for polarizations in Fig. 4(b, d), the peak PLD (0.71 kW/m^3,0.61 kW/m^3) in hair was 43.04% and 47.4% lower than the skin surface whereas it was 67.6% and 49.7% higher in the sebaceous gland (3.9 kW/m^3, 2.5 kW/m^3).

Aside from the higher E inside the hair, the local spikes in E (57.2 V/m) and PLD (61.53 kW/m^3) around the hair for the polarization shown in Fig. 4(c, d) were roughly 37.5% and 60.9% greater compared to that in surrounding skin. On the other hand, for the polarization shown in Fig. 4(a, b), the local E (16.01 V/m) and PLD (4.82 kW/m^3) in the immediate vicinity of the hair was 53.7% and 78.5% smaller than in the surrounding skin. These abrupt local enhancements and reductions were because hair with an electrically small diameter acted as an electric dipole with surface charges induced at its boundaries depending on the polarization.

In contrast, the high-water content appendages, such as arrector pili muscle and capillaries associated with sebaceous gland, exhibited the peak E (28.9 V/m and 24.8 V/m), which was 11.2% and 10.2% lower than in surrounding skin for the polarization shown in Fig. 4(a). Conversely, the corresponding PLD in muscle (21.9 kW/m^3) and capillaries (16.83 kW/m^3) was 9.6% and 14.7% more intense than in surrounding skin [Fig. 4(b)]. Furthermore, for the orientation of E displayed in Fig. 4(c), the maximal E was 9.2% lower in arrector pili muscle (29.1 V/m) and 16.1% higher in capillaries of sebaceous gland (33.1 V/m) compared to that in surrounding skin. The PLD associated with the muscle (22.3 kW/m^3) and capillaries (30.03 kW/m^3) in this case was 13.5% and 51.6% higher than that in surrounding skin. The notable enhancement of power absorption inside the capillaries for the latter polarization is explicable by charge accumulation at the interface of sebaceous gland due to the discontinuity of normal electric displacement vector D, which results in discontinuity in E equal to the permittivity of sebaceous material. Notice that maximal PLD (22 kW/m^3) inside the arrector pili muscle was 94% higher than the skin surface whereas peak E (29 V/m) was 24% lower for both polarizations.

For both polarizations shown in Fig. 4, the E in arrector pili muscle and capillaries around the hair follicle attenuated by 48.3% (29 $\Rightarrow$ 15 V/m) and 50% (20 $\Rightarrow$ 10 V/m) over a length of 270 µm and 325 µm, respectively. The higher conductivity of blood and muscle was the critical factor that led to this attenuation. The corresponding PLD in the arrector pili muscle (22 kW/m^3 to 6 kW/m^3) and capillaries supplying the hair follicle (11.5 kW/m^3 to 2.9 kW/m^3) decreased by 72.7% and 74.8%.

The variation of E with depth (640 µm) in hair (57 $\Rightarrow$ 12 V/m) for both polarizations was 78.9%. The E in the skin (9.2 V/m) near the bottom of hair root was 23.3% lower than that inside the hair. Thus, the low water content hair provides
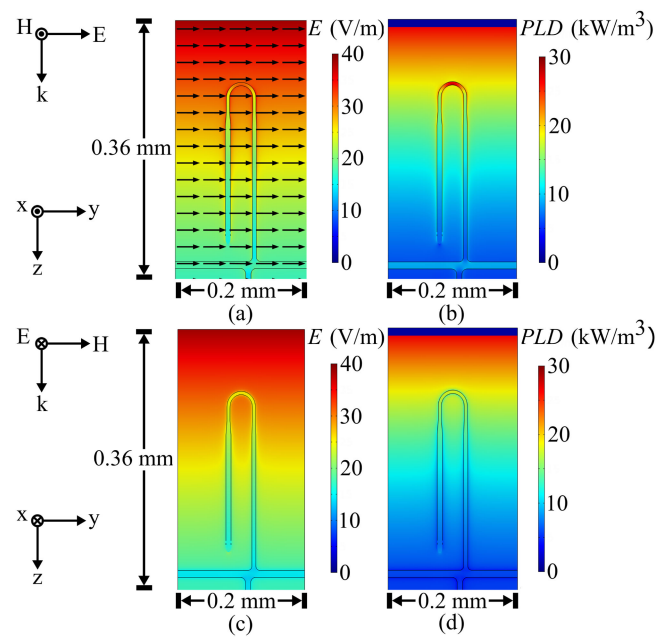

FIGURE 5. Cutaneous microvasculature: (a), (c) E distribution; (b), (d) PLD distribution.

a natural route for the penetration of 60 GHz signal to deeper more vulnerable regions of skin with less attenuation. The PLD also followed a similar trend i.e., attenuation of PLD in hair (0.5 $\Rightarrow$ 0.02 kW/m^3) was 96% over a length of 640 µm.

D. CUTANEOUS MICROVASCULATURE

Fig. 5 shows E and PLD in an orthogonal cut through the section of the cutaneous microvasculature located above superficial plexus. The local peak (26.9 kW/m^3) of PLD inside the leading segment of the capillary loop is the most striking feature of the results shown in Fig. 5(b) and was approximately 30.6% higher than the surrounding skin. This is explicable by the higher conductivity of blood in comparison to skin as E in top segment of the capillary loop (31.4 V/m) was similar to the surrounding skin due to the conservation of tangential component of E across the interface. Note that the peak PLD inside the capillary loop was 95.4% higher than at the skin surface. Contrarily, the maximal E (31.4 V/m) induced in the capillary loop was 18.1% lower than at the skin surface. The results also showed remarkably high (peak = 30.9%) PLD (24.9 kW/m^3) at the vertical boundaries of capillary loop/skin compared to the surrounding skin. This was because the step discontinuity in permittivity led to charge accumulation at the boundary and resulted in strong concentration (peak = 16.9%) of E (36.4 V/m) in comparison to surrounding skin. The aforementioned abrupt changes in PLD highlight that pericytes and endothelial cells, which line the blood vessels, are exposed to higher PLD compared to surrounding skin cells. Lastly, the average PLD (10.63 kW/m^3) and E (19.61 V/m) in the arterial limb was 0.7% and 0.33% higher than in venous limb of the capillary suggesting a weak dependence on their diameter.

Similarly, compared to surrounding skin, *PLD* was predominantly enhanced (31.4% and 31.5%) in arteries of superficial (9.05 kW/m^3) and deep plexus (0.56 kW/m^3) [Fig. 5(b)]. Note that the difference between *E* inside the superficial (18.19 V/m) and deep (4.53 V/m) plexus compared to surrounding skin was less than 0.1%. For most part, *PLD* and *E* were uniform in the transverse cross-sections of the blood vessels except directly under the vertical joints that connected blood vessels with each other.

For the polarization shown in Fig. 5(d), it was clear that maximum *PLD* in the capillary loop (18.7 kW/m^3) was roughly 5% lower than surrounding skin. This was because the boundary conditions in this orientation required |*E*| to alter inversely with the permittivity of the corresponding domains. In other words, peak *E* inside the capillary loop (25.51 V/m) was 19.2% lower than surrounding skin. Moreover, in contrast to the polarization shown in Fig. 5(b), *PLD* on the surface of the vertical segments of the capillary loop (12.1 kW/m^3) was 29.6% lower than the surrounding skin [Fig. (c)]. This was due to formation of electric dipole around the capillary loop with a minimum *E* (25.4 V/m) at the lateral sides (16.1% lower than in surrounding skin).

Likewise, due to weak *E* coupling, the maximal *PLD* inside the arteries (5.9 kW/m^3) and veins (5.3 kW/m^3) of superficial plexus was diminished by 5.5% and 5.36% compared to the surrounding skin [Fig. 5(c, d)]. Similarly, the maximal *PLD* in arteries (0.37 kW/m^3) and veins (0.3 kW/m^3) of deep plexus was 7.3% and 6.5% lower than in surrounding skin. The corresponding reduction of *E* in superficial (19.4 V/m) and deep (3.7 V/m) plexus was observed to be 19.4% and 20.2% in comparison to surrounding skin.

Lastly, *PLD* (4.8 ⇒ 0.4 kW/m^3) inside arteries connecting superficial plexus to deep dermal plexus exhibited a general decline (92%) along the propagation path (0.58 mm) for both polarizations (data omitted for brevity). This was due to a rapid decay (71%) of *E* (13.3 ⇒ 3.8 V/m) in highly lossy blood. The results were similar for both polarizations because *E* was directed normal to the lateral surface of blood vessels.

E. ECCRINE SWEAT GLANDS

Fig. 6 shows that the precise location of the maximal *PLD* (45.2 kW/m^3) occurred in the portion of acrosyringium, which was parallel to the applied *E*, and was roughly 45% higher than that in surrounding skin for both polarizations. The local enhancement in power dissipation was due to a higher conductivity of sweat in comparison to surrounding skin. The corresponding peak *E* (34.6 V/m) approached *E* (5% difference) in surrounding skin due to requirements imposed on tangential *E* to be continuous across the interface. Note that for both polarizations, the maximal *PLD* in the acrosyringium (45.2 kW/m^3) was 97.2% higher than at the skin surface. Contrarily, the peak *E* induced in acrosyringium (34.6 V/m) was 9% lower than at the skin surface.

Similarly, for the polarization displayed in Fig. 6(d), the maximal *PLD* (9.3 kW/m^3) inside the spiraling blood vessel was 3.2% higher than in surrounding skin. Contrarily, for the
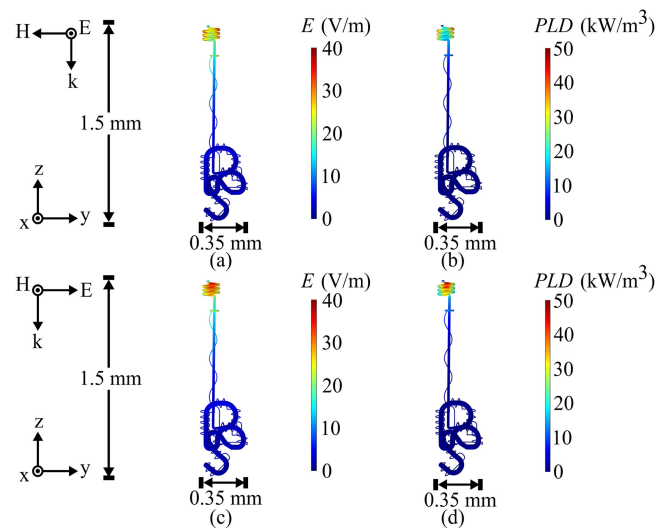

FIGURE 6. Eccrine sweat gland: (a), (c) *E* distribution; (b), (d) *PLD* distribution.

polarization shown in Fig. 6(b), the peak *PLD* (8.8 kW/m^3) inside the blood vessel was 2.94% lower than in surrounding skin. The higher power loss in the former case was because of stronger *E* (18.4 V/m) due to the slanting profile of the blood vessel with respect to the applied *E* (21.9 V/m) [Fig. 6(c)]. Stated differently, the *E* (17.9 V/m) was relatively less strong in Fig 6(b) as the blood vessel presents a less slant profile to the applied *E* (21.9 V/m). Thus, for normal incidence, higher power loss occurs in the blood vessels which transverse the skin at an oblique angle in comparison to vertical vessels.

In the straight duct, there was a progressive reduction of *PLD* (15 ⇒ 0.2 kW/m^3 i.e., 98.7%) and *E* (20 ⇒ 2.3 V/m i.e., 88%) over a length of 1 mm for both polarizations due to highly dissipative sweat. Similarly, the *E* (18 ⇒ 4.4 V/m) and *PLD* (9 ⇒ 0.5 kW/m^3) inside the blood vessels (660 μm long) spiraling along the sweat duct also decreased by 75% and 94%.

It is also worthwhile to mention that at the midpoint of the straight duct *PLD* (1.73 kW/m^3) was 7% lower than in surrounding skin for both orientations of *E*. Similarly, *E* (6.7 V/m) was 32.1% lower than surrounding skin owing to higher attenuation inside the sweat. Contrarily, at the same depth, *PLD* (1.88 kW/m^3) inside blood vessels was 1% higher than in surrounding skin. The key factor responsible for this was the higher conductivity of blood vs skin and it led to 16% lower *E* (8.4 V/m) in blood vessel compared to surrounding skin. Note that *PLD* and *E* were uniform in the transverse sections of the straight duct and associated blood vessels.

Lastly, for the polarization case in Fig 6(a, b), the average *PLD* (0.178 kW/m^3) and *E* (2.06 V/m) inside the secretory coil located at the end of the dermis was 19.5% and 24.3% lower than that in its associated blood vessels. A different picture emerged from Fig. 6(c, d) where secretory coil's average *PLD* (0.247 kW/m^3) was 13.3% higher than that of blood vessels. This was primarily because the orientation of
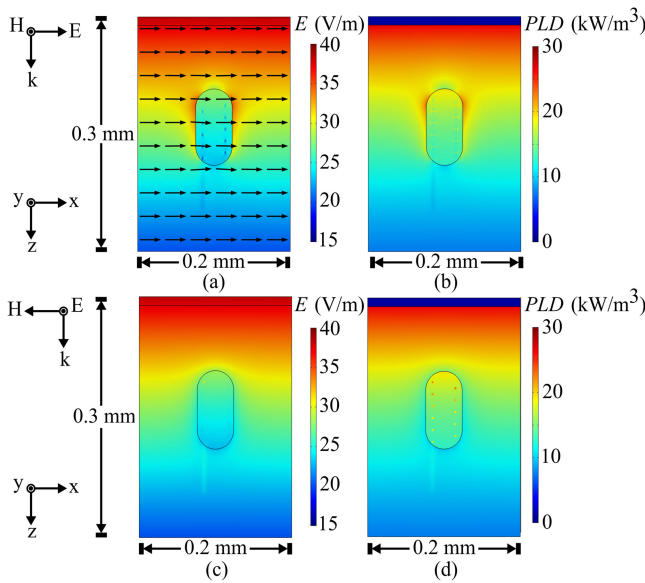
FIGURE 7. Meissner corpuscle: (a), (c) *E* distribution; (b), (d) *PLD* distribution.

FIGURE 8. Pacinian corpuscle: (a), (c) *E* distribution; (b), (d) *PLD* distribution.

the secretory coils was relatively parallel to applied *E* in the latter case and led to comparatively stronger coupling. In other words, average *E* inside the blood vessels (2.69 V/m) was 10.4% higher than that of the secretory coil.

Despite the high conductivity of sweat, the peaks in *PLD* were also localized in the zones immediately around the portion of duct normal to applied *E* for both polarizations (data omitted for brevity). For instance, the *PLD* (42 kW/m^3) near the interface of the top segment of the sweat duct was 50% higher than inside the same duct (21 kW/m^3). This is because of the existence of the charge distributions at such interfaces which is necessary to satisfy the charge conservation ($\sigma_1 E_1^\perp - \sigma_2 E_2^\perp = j\omega\rho_s$) and Gauss's law. Consequently, *E* (47 V/m) at the aforementioned interface was also 50% higher compared to internal *E* of the duct. Due to dissipation of energy along the boundary of sweat duct, the cells lining the duct would be subjected to a higher intensity mmWave radiation than cells inside them.

F. MEISSNER CORPUSCLE

Fig. 7(a) depicts that the *PLD* maxima (19.01 kW/m^3) inside the frontal hemispherical lumen of Meissner corpuscle was 1.7% greater than in surrounding skin because of its higher conductivity. Opposite was true for *E* (28.3 V/m) which was 10.1% lower than in surrounding skin. Due to geometrical symmetry of Meissner corpuscle, the polarization dependence of *PLD* and *E* was weak (0.01%) [Fig. 7(c, d)]. Note that the maximal *PLD* inside the lumen of Meissner corpuscle was 93.4% higher than the skin surface whereas maximal *E* (28.32 V/m) inside it was 25.8% lower.

Moreover, *PLD* (19.01 kW/m^3 to 12.7 kW/m^3) and *E* (28 V/m to 23 V/m) tapered off by 33% and 18% along the propagation route inside the Meissner corpuscle for both
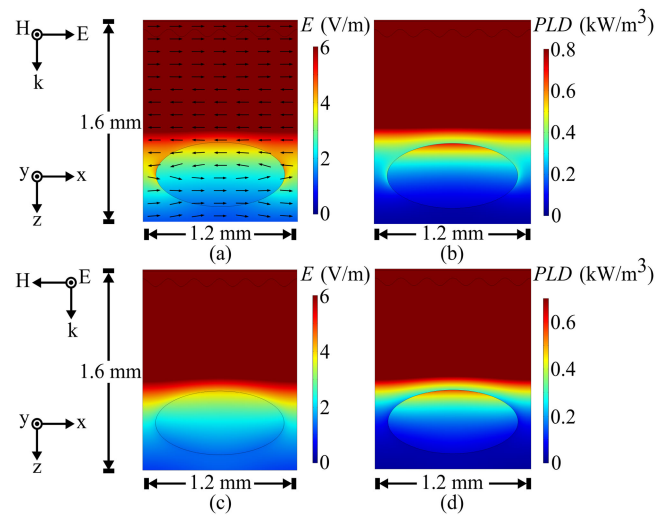
polarizations. A closer examination of Fig. 7(d) revealed that the peak *PLD* (21.2 kW/m^3) inside the axon of Meissner corpuscle was roughly 22.9% higher compared to its lumen. This was because *E* (26.2 V/m) parallel to the axon interface remained continuous in conformity with the boundary conditions for tangential *E*. However, in spite of the high conductivity of axoplasm, the maximal *PLD* (16.91 kW/m^3) inside it in Fig. 7(b) was only 0.8% higher than in surrounding lumen of Meissner corpuscle. This was due to the reduction of induced *E* (23.4 V/m versus 26.6 V/m) by 11.9% inside the axoplasm in accordance with boundary conditions on the normal component of incident *E*. Furthermore, Fig. 7(a, b) show that the highest *E* (34.7 V/m) and *PLD* (22.6 kW/m^3) around the fringes of the Meissner corpuscle were 12.7% and 23.8% higher than unperturbed values in skin. Contrarily, the peak *E* (26.8 V/m) and *PLD* (13.5 kW/m^3) along the top boundaries of the Meissner corpuscle in Fig. 7(c, d) were 9.7% and 18.5% lower compared to surrounding skin because of formation of an electric dipole around it. Finally, in the transverse sections of the Meissner corpuscle, the *E* and *PLD* were not uniform due to the presence of the axon.

G. PACINIAN CORPUSCLE

Fig. 8(a) shows that the highest *PLD* (0.69 kW/m^3) was localized at the front surface of the Pacinian corpuscle and was roughly 32.5% higher than the surrounding skin mainly due to significantly higher conductivity of the Pacinian corpuscle. The peak *E* (4.53 V/m) at the frontal surface corresponded closely (9.66% difference) to that in surrounding skin due the continuity of the tangential components of the incident *E*. Alternatively, for the polarization displayed in Fig. 8(d), the peak *PLD* (0.575 kW/m^3) was only 20.5% higher than the surrounding skin. The absorption was higher in the former case because incident *E* was parallel to the longest dimension of the corpuscle, which resulted in stronger *E*. Conversely,

the maximal E (4.1 V/m) in Fig. 8(c) was 16.9% lower than in surrounding skin. Notice that the maximal *PLD* in the Pacinian corpuscle was 44.1% and 54.04% lower than at the skin surface for the polarizations displayed in Fig. 8(b, d), respectively. Similarly, maximal E induced in the Pacinian corpuscle was also 88.2% and 89.3% lower than at the skin surface [Fig. 8(a, c)].

Moreover, *PLD* and E underwent severe attenuation inside the Pacinian corpuscle due to its higher water content. The reduction in *PLD* (0.06 kW/m^3 [Fig. 8(b)] and 0.08 kW/m^3 [Fig. 8(d)]) and E (1.3 V/m [Fig. 8(a)] and 1.6 V/m [Fig. 8(c)]) exceeded 88% and 65% at its trailing surface for both polarizations. Lastly, the peak *PLD* and E due the dielectric discontinuity of the Pacinian corpuscle was always along the axis parallel to the incident E. For instance, the peak *PLD* (0.36 kW/m^3) and E (4.35 V/m) for the polarization in Fig. 8(a, b) along the major axis of the Pacinian corpuscle was roughly 52.4% and 31.05% higher than in surrounding skin. On the contrary, for the orientation of E displayed in Fig. 8(c, d), the peak *PLD* (0.097 kW/m^3) and E (2.28 V/m) was approximately 36.5% and 20.3% lower than in surrounding skin.

IV. CONCLUSION AND DISCUSSION

In this study, high-resolution 3D models of a complete set of human skin sub-structures (blood vessels, nerve fibers, lymphatic vessels, eccrine sweat glands, sebaceous glands, hair, arrector pili muscle, Pacinian corpuscle, and Meissner corpuscle) were developed based on anatomical data. These models were used to investigate local power distribution in human skin appendages at 60 GHz.

The maximum *PLD* (45.2 kW/m^3) was observed in the portion of the acrosyringium parallel to the incident E and was about 45% higher than surrounding skin, mainly due to high water content of sweat. The epidermal axons and Pacinian corpuscle were the skin substructures with second (37.9% i.e., 42.5 kW/m^3) and third (32.5% i.e., 0.69 kW/m^3) highest *PLD* compared to the surrounding skin whereas the *PLD* in blood capillary, axon of Meissner corpuscle, lymphatic capillary and arrector pili muscle was 30.6% (26.9 kW/m^3), 23.3% (21.2 kW/m^3), 20% (20.2 kW/m^3) and 13.5% (22.3 kW/m^3) higher than surrounding skin. Note that some reports suggested that the pain-relieving effect of mmWaves could pass through nerve endings of skin [80]. Our results demonstrate relatively high exposure levels in $A\delta$ and C fibers known to be involved in pain detection.

Although, the maximum E inside hair (65.7 V/m) and sebaceous gland (36.8 V/m) was 45.05% and 36.96% higher than in surrounding skin, the corresponding *PLD* (0.71 kW/m^3 and 3.9 kW/m^3) was 97.1% and 61.8% lower due to their lower water content. Moreover, the higher E detected inside hair suggests that hair provides a natural route for the penetration of 60 GHz signal to deeper regions of skin.

The heterogeneous skin model also revealed strikingly higher (23.8%-60.9%) local *PLD* (22.6-61.53 kW/m^3) at skin appendages-skin interfaces compared to the surrounding homogeneous skin due to the dielectric discontinuities. This

suggests that cells lining (epithelial, endothelial, pericytes, etc.) the different skin appendages are exposed to higher electromagnetic power and potentially subject to higher local heating (thermal analysis is out of the scope of this study and constitutes one of its perspectives).

This study is one of the very first attempts towards understanding of microscale power deposition in skin at mmWave frequencies. Generic models of the skin sub-structures based on the electron microscopy images provide an insight into micro-scale absorption mechanisms in cutaneous layers and reveal the potential capability of mmWaves to selectively target specific skin appendages such as nerves or capillaries. Further refinement of such models based on stochastic approach and recent advancements in non-invasive imaging techniques (e.g., optical coherence tomography [18]) would allow to assess interindividual variability. Additionally, the swift progress towards accurately mapping skin water content at microscale and nanoscale level using Raman microspectroscopy [81], [82] and low-loss electron energy-loss spectroscopy [83] would further improve the dielectric dispersive models of skin appendages and help to elucidate specific absorption sites. Lastly, an experimental direct or indirect validation of the reported results could provide further insight into numerical results, the accuracy of which is directly related to the realism of the model physical properties as well as to the precision of computational technique.

REFERENCES

[1] W. Tang *et al.*, "Wireless communications with reconfigurable intelligent surface: Path loss modeling and experimental measurement," *IEEE Trans. Wireless Commun.*, vol. 20, no. 1, pp. 421–439, Jan. 2021.

[2] Q. Qi, X. Chen, C. Zhong, and Z. Zhang, "Integrated sensing, computation and communication in B5G cellular Internet of Things," *IEEE Trans. Wireless Commun.*, vol. 20, no. 1, pp. 332–344, Jan. 2021.

[3] S. Verploegh, M. Pinto, L. Marzall, D. Martin, G. Lasser, and Z. Popović, "Analysis of process variations in W-band GaN MMIC PAs using nonparametric statistics," *IEEE Trans. Microw. Theory Techn.*, vol. 69, no. 4, pp. 2304–2318, Apr. 2021.

[4] D. A. Pham, E. Park, H. L. Lee, and S. Lim, "High gain and wideband metasurfaced magnetoelectric antenna for WiGig applications," *IEEE Trans. Antennas Propag.*, vol. 69, no. 2, pp. 1140–1145, Feb. 2021.

[5] H. Yin, L. Zhang, and S. Roy, "Multiplexing URLLC traffic within eMBB services in 5G NR: Fair scheduling," *IEEE Trans. Commun.*, vol. 69, no. 2, pp. 1080–1093, Feb. 2021.

[6] R. Liu, G. Yu, J. Yuan, and G. Y. Li, "Resource management for millimeter-wave ultra-reliable and low-latency communications," *IEEE Trans. Commun.*, vol. 69, no. 2, pp. 1094–1108, Feb. 2021.

[7] A. Christ *et al.*, "The virtual family – Development of surface-based anatomical models of two adults and two children for dosimetric simulations," *Phys. Med. Biol.*, vol. 55, no. 2, pp. N23–N38, 2010.

[8] H. Zaidi and B. M. W. Tsui, "Review of computational anthropomorphic anatomical and physiological models," *Proc. IEEE*, vol. 97, no. 12, pp. 1938–1953, 2009.

[9] A. Pellegrini *et al.*, "Antennas and propagation for body-centric wireless communications at millimeter-wave frequencies: A review [Wireless Corner]," *IEEE Antennas Propag. Mag.*, vol. 55, no. 4, pp. 262–287, Oct. 2013.

[10] O. P. Gandhi and A. Riazi, "Absorption of millimeter waves by human beings and its biological implications," *IEEE Trans. Microw. Theory Techn.*, vol. 34, no. 2, pp. 228–235, Feb. 1986.

[11] S. I. Alekseev, A. A. Radzievsky, M. K. Logani, and M. C. Ziskin, "Millimeter wave dosimetry of human skin," *Bioelectromagnetics*, vol. 29, no. 1, pp. 65–70, Jan. 2008.

[12] N. Chahat, M. Zhadobov, and R. Sauleau, "Broadband tissue-equivalent phantom for BAN applications at millimeter waves," *IEEE Trans. Microw. Theory Techn.*, vol. 60, no. 7, pp. 2259–2266, May 2012.

[13] A. R. Guraliuc, M. Zhadobov, O. D. Sagazan, and R. Sauleau, "Solid phantom for body-centric propagation measurements at 60 GHz," *IEEE Trans. Microw. Theory Techn.*, vol. 62, no. 6, pp. 1373–1380, May 2014.

[14] S. I. Alekseev and M. C. Ziskin, "Millimeter-wave absorption by cutaneous blood vessels: A computational study," *IEEE Trans. Biomed. Eng.*, vol. 56, no. 10, pp. 2380–2388, Oct. 2009.

[15] S. I. Alekseev and M. C. Ziskin, "Distortion of millimeter-wave absorption in biological media due to presence of thermocouple and other objects," *IEEE Trans. Biomed. Eng.*, vol. 48, no. 9, pp. 1013–1019, Sep. 2001.

[16] Y. Feldman, A. Puzenko, P. B. Ishai, A. Caduff, and A. J. Agranat, "Human skin as arrays of helical antennas in the millimeter and submillimeter wave range," *Phys. Rev. Lett.*, vol. 100, 2008, Art. no. 128102.

[17] I. Hayut, A. Puzenko, P. B. Ishai, A. Polsman, A. J. Agranat, and Y. Feldman, "The helical structure of sweat ducts: Their influence on the electromagnetic reflection spectrum of the skin," *IEEE Trans. THz Sci. Technol.*, vol. 3, no. 2, pp. 207–215, Mar. 2013.

[18] N. Betzalel, Y. Feldman, and P. B. Ishai, "The modeling of the absorbance of sub-THz radiation by human skin," *IEEE Trans. THz Sci. Technol.*, vol. 7, no. 5, pp. 521–528, Sep. 2017.

[19] M. Huzaira, F. Rius, M. Rajadhyaksha, R. R. Anderson, and S. González, "Topographic variations in normal skin, as viewed by in vivo reflectance confocal microscopy," *J. Invest. Dermatol.*, vol. 116, no. 6, pp. 846–852, 2001.

[20] Y. Lee and K. Hwang, "Skin thickness of Korean adults," *Surg. Radiol. Anat.*, vol. 24, no. 3/4, pp. 183–189, Jan. 2002.

[21] K. Sauermann et al., "Age related changes of human skin investigated with histometric measurements by confocal laser scanning microscopy in vivo," *Skin Res. Technol.*, vol. 8, no. 1, pp. 52–56, Feb. 2002.

[22] J. C. McArthur, E. A. Stocks, P. Hauer, D. R. Cornblath, and J. W. Griffin, "Epidermal nerve fiber density: Normative reference range and diagnostic efficiency," *Arch. Neurol.*, vol. 55, no. 12, pp. 1513–1520, Dec. 1998.

[23] A. S. Ross, F. M. Whalen, R. Elenitas, X. Xu, A. B. Troxel, and C. D. Schmults, "Diameter of involved nerves predicts outcomes in cutaneous squamous cell carcinoma with perineural invasion: An investigator-blinded retrospective cohort study," *Dermatol. Surg.*, vol. 35, no. 12, pp. 1859–1866, Dec. 2009.

[24] C. M. Reinisch and E. Tschachler, "The dimensions and characteristics of the subepidermal nerve plexus in human skin-terminal schwann cells constitute a substantial cell population within the superficial dermis," *J. Dermatol. Sci.*, vol. 65, no. 3, pp. 162–169, Mar. 2012.

[25] R. Kitatani, M. Yamada, M. Kamio, and H. Nagai, "Length is associated with pain: Jellyfish with painful sting have longer nematocyst tubules than harmless jellyfish," *PLoS One*, vol. 10, no. 8, pp. 1–13, Aug. 2015.

[26] E. Tschachler, C. M. Reinisch, C. Mayer, K. Paiha, H. Lassmann, and W. Weninger, "Sheet preparations expose the dermal nerve plexus of human skin and render the dermal nerve end organ accessible to extensive analysis," *J. Invest. Dermatol.*, vol. 122, no. 1, pp. 177–182, Jan. 2004.

[27] E. R. Kandel, J. H. Schwartz, T. M. Jessell, S. A. Siegelbaum, and A. J. Hudspeth, *Principles of Neural Science*, 5th ed. New York, NY, USA: McGraw-Hill, 2000, pp. 475–497.

[28] R. P. Arthur and W. B. Shelly, "The innervation of human epidermis," *J. Invest. Dermatol.*, vol. 32, no. 3, pp. 397–411, Mar. 1959.

[29] M. Hilliges, L. Wang, and O. Johansson, "Ultrastructural evidence for nerve fibers within all vital layers of the human epidermis," *J. Invest. Dermatol.*, vol. 104, no. 1, pp. 134–137, Jan. 1995.

[30] T. J. Ryan, "Structure and function of lymphatics," *J. Invest. Dermatol.*, vol. 93, no. 2, pp. S18–S24, Aug. 1989.

[31] M. W. Greaves and S. Shuster, *Pharmacology of the Skin I: Pharmacology of Skin Systems Autocoids in Normal and Inflamed Skin*. New York, NY, USA: Springer, 1989, pp. 89–116.

[32] D. Lubach, A. W. Schulz, D. Neukam, and S. Nissen, "The extension technique: A new method of demonstrating initial lymph vessels in excised human skin," *Brit. J. Dermatol.*, vol. 123, no. 2, pp. 179–185, Aug. 1990.

[33] X. Wang et al., "A three-dimensional atlas of human dermal leukocytes, lymphatics, and blood vessels," *J. Invest. Dermatol.*, vol. 134, no. 4, pp. 965–974, Apr. 2014.

[34] D. Lubach, S. Stuwe, S. Nissen, and D. B. V. Rautenfeld, "Histological demonstration of initial lymphatics in human skin: Comparison between different extension techniques," *Arch. Dermatol. Res.*, vol. 283, no. 4, pp. 240–245, Apr. 1991.

[35] A. Rossi et al., "Lymphatic and blood vessels in scleroderma skin, a morphometric analysis," *Hum. Pathol.*, vol. 41, no. 3, pp. 366–374, Mar. 2010.

[36] V. P. Eroschenko and M. S. Di Fiore, *DiFiore's Atlas of Histology With Functional Correlations*, 11th ed. Philadelphia, PA, USA: Lippincott, Williams & Wilkins, 2013, pp. 213–234.

[37] A. Vogt et al., "Morphometry of human terminal and vellus hair follicles," *Exp. Dermatol.*, vol. 16, no. 11, pp. 946–950, Nov. 2007.

[38] N. Otberg, H. Richter, H. Schaefer, U. B. Peytavi, W. Sterry, and J. Lademann, "Variations of hair follicle size and distribution in different body sites," *J. Invest. Dermatol.*, vol. 122, no. 1, pp. 14–19, Jan. 2004.

[39] C. C. Robbins, *Chemical and Physical Behaviour of Human Hair*, 4th ed. Berlin, Germany: Springer-Verlag, 2000, pp. 537–640.

[40] B. Buffoli et al., "The human hair: From anatomy to physiology," *Int. J. Dermatol.*, vol. 53, no. 3, pp. 331–341, Mar. 2014.

[41] M. R. Avram and N. E. Rogers, "Hair transplantation for men," *J. Cosmetic Laser Therapy*, vol. 10, no. 3, pp. 154–160, Jan. 2008.

[42] L. Mecklenburg, M. Linek, and D. J. Tobin, Eds., *Hair Loss Disorders in Domestic Animals*. New York, NY, USA: Wiley, 2009, pp. 43–62.

[43] F. H. Sakamoto et al., "Selective photothermolysis to target sebaceous glands: Theoretical estimation of parameters and preliminary results using a free electron laser," *Lasers Surg. Med.*, vol. 44, no. 2, pp. 175–183, Feb. 2012.

[44] S. G. Johnsen and J. E. Kirk, "The number, distribution and size of the sebaceous glands in the dorsal region of the hand," *Anat. Rec.*, vol. 112, no. 4, pp. 725–735, Apr. 1952.

[45] L. N. Michelson et al., "The quantification and distribution of nasal sebaceous glands using image analysis," *Aesthetic Plast. Surg.*, vol. 20, no. 4, pp. 303–309, Jul. 1996.

[46] R. A. Ellis and G. Moretti, "Vascular patterns associated with catagen hair follicles in the human scalp," *Ann. New York Acad. Sci.*, vol. 83, no. 3, Nov. 1959, pp. 448–457.

[47] W. Montagna and P. F. Parakkal, *The Structure and Function of Skin*, 3rd ed. New York, NY, USA: Academic, pp. 280–411, 1974.

[48] W. Montagna, A. M. Kligman, and K. S. Carlisle, *Atlas of Normal Human Skin*. Philadelphia, PA, USA: Springer Science & Business Media, 2012, pp. 1–94.

[49] I. M. Braverman, "Ultrastructure and organization of the cutaneous microvasculature in normal and pathologic states," *J. Invest. Dermatol.*, vol. 93, no. 2, pp. 2S–9S, Aug. 1989.

[50] C. Bertrand and P. Corcuff, "In vivo spatio-temporal visualization of the human skin by real-time confocal microscopy," *Scanning*, vol. 16, no. 3, pp. 150–154, 1994.

[51] M. E. Tavakol, A. Fatemi, A. Karbalaie, Z. Emrani, and B. E. Erlandsson, "Nailfold capillaroscopy in rheumatic diseases: Which parameters should be evaluated?," *BioMed Res. Int.*, vol. 2015, pp. 1–17, 2015.

[52] O. Gans and G. K. Steigleder, *Normale Und Pathologische Anatomie Der Haut I*. Berlin, Germany: Springer, 1968, pp. 529–534.

[53] P. Agache, F. Fanian, H. I. Maibach, and P. Humbert, *Agache's Measuring the Skin*, 2nd ed. Cham, Switzerland: Springer, 2017, pp. 549–562.

[54] G. Cevc and U. Vierl, "Spatial distribution of cutaneous microvasculature and local drug clearance after drug application on the skin," *J. Controlled Release*, vol. 118, no. 1, pp. 18–26, Mar. 2007.

[55] K. Hwang and S. H. Baik, "Distribution of hairs and sweat glands on the bodies of Korean adults: A morphometric study," *Cells Tissues Organs*, vol. 158, no. 2, pp. 112–120, May 1997.

[56] K. Wilke, A. Martin, L. Terstegen, and S. S. Biel, "A short history of sweat gland biology," *Int. J. Cosmetic Sci.*, vol. 29, no. 3, pp. 169–179, Jun. 2007.

[57] A. L. Mescher, *Junqueira's Basic Histology: Text and Atlas*, 13th ed. New York, NY, USA: McGraw-Hill Medical, 2013, pp. 364–384.

[58] V. Cantoni, V. D. Gesu, A. Setti, and D. Tegolo, *Human and Machine Perception: Information Fusion*. New York, NY, USA: Springer, 1997, pp. 87–107.

[59] J. E. Calonje, T. Brenn, A. J. Lazar, and S. Billings, *McKee's Pathology of the Skin*, 2 Volume Set E-Book, 4th ed. Amsterdam, The Netherlands: Elsevier Health Sciences, 2018, pp. 1–31.

[60] J. Bell, S. Bolanowski, and M. H. Holmes, "The structure and function of pacinian corpuscles: A review," *Prog. Neurobiol.*, vol. 42, no. 1, pp. 79–128, Jan. 1994.

[61] K. O. Johnson and G. D. Lamb, "Neural mechanisms of spatial tactile discrimination: Neural patterns evoked by braille-like dot patterns in the monkey," *J. Physiol.*, vol. 310, no. 1, pp. 117–144, Jan. 1981.

[62] S. I. Alekseev and M. C. Ziskin, "Human skin permittivity determined by millimeter wave reflection measurements," *Bioelectromagnetics*, vol. 28, no. 5, pp. 331–339, 2007.

[63] S. Gabriel, R. W. Lau, and C. Gabriel, "The dielectric properties of biological tissues: III. Parametric models for the dielectric spectrum of tissues," *Phys. Med. Biol.*, vol. 41, no. 11, pp. 2271–2293, Nov. 1996.

[64] M. C. Ziskin, S. I. Alekseev, K. R. Foster, and Q. Balzano, "Tissue models for RF exposure evaluation at frequencies above 6 GHz," *Bioelectromagnetics*, vol. 39, no. 3, pp. 173–189, Feb. 2018.

[65] W. J. Ellison, "Permittivity of pure water, at standard atmospheric pressure, over the frequency range 0-25 THz and the temperature range 0–100°C," *J. Phys. Chem. Ref. Data*, vol. 36, pp. 1–8, 2007.

[66] H. Fischer, I. Polikarpov, and A. F. Craievich, "Average protein density is a molecular-weight-dependent function," *Protein Sci.*, vol. 13, no. 10, pp. 2825–2828, Oct. 2004.

[67] R. Wagner, *Elements of Physiology: For the Use of Students, and With Particular Reference to the Wants of Practitioners*. London, U.K.: Sherwood, Gilbert, & Piper, 1841, pp. 267–272.

[68] W. J. Jr Adelman, J. M. Arnold, and D. L. Gilbert, *Squid as Experimental Animals*. New York, NY, USA: Springer, 2013, pp. 235–302.

[69] V. P. Dadykin, *Growing Plants in Space*. Washington, DC, USA: NASA, 1972, pp. 1–76.

[70] L. D. Bulkley, *Acne: Its Etiology, Pathology and Treatment*. New York, NY, USA: Churchill, 1885, pp. 1–19.

[71] J. Jamart, M. Djaghloul, J. M. Bergheau, and H. Zahouani, "Effect of water desorption on the rheology and dynamic response of human hair to a non-contact impact," *J. Mech. Behav. Biomed. Mater.*, vol. 46, pp. 176–183, Jun. 2015.

[72] R. M. LoPachin Jr., E. J. Lehning, E. C. Stack, S. J. Hussein, and A. J. Saubermann, " 2, 5-hexanedione alters elemental composition and water content of rat peripheral nerve myelinated axons," *J. Neurochemistry*, vol. 63, no. 6, pp. 2266–2278, Dec. 1994.

[73] E. J. Lehning, P. K. Stys, and R. M. LoPachin Jr., "Reoxygenation of anoxic peripheral nerve myelinated axons promotes re-establishment of normal elemental composition," *Brain Res.*, vol. 715, no. 1/2, pp. 189–196, Apr. 1996.

[74] H. P. Schwan, "Electrical properties of bound water," *Ann. New York Acad. Sci.*, vol. 125, no. 2, pp. 344–354, Oct. 1965.

[75] J. L. Schepps and K. R. Foster, "The UHF and microwave dielectric properties of normal and tumour tissues: Variation in dielectric properties with tissue water content," *Phys. Med. Biol.*, vol. 25, no. 6, pp. 1149–1159, Nov. 1980.

[76] B. E. Pennock and Herman P. Schwan, "Further observations on the electrical properties of hemoglobin-bound water," *J. Phys. Chem.*, vol. 73, no. 8, pp. 2600–2610, Aug. 1969.

[77] T. Hanai, K. Asami, and N. Koizumi, "Dielectric theory of concentrated suspensions of shell-spheres in particular reference to the analysis of biological cell suspensions," *Bull. Inst. Chem. Res., Kyoto Univ.*, vol. 57, pp. 297–305, 1979.

[78] K. Asami, "Characterization of heterogeneous systems by dielectric spectroscopy," *Prog. Polym. Sci.*, vol. 27, no. 8, pp. 1617–1659, Oct. 2002.

[79] G. Sacco, S. Pisa, and M. Zhadobov, "Age-dependence of electromagnetic power and heat deposition in near-surface tissues in emerging 5G bands," *Sci. Rep.*, vol. 11, no. 1, pp. 1–11, 2021.

[80] A. A. Radzievsky, M. A. Rojavin, A. Cowan, and M. C. Ziskin, "Suppression of pain sensation caused by millimeter waves: A double-blinded, cross-over, prospective human volunteer study," *Anesth. Analg.*, vol. 88, no. 4, pp. 836–840, Apr. 1999.

[81] D. M. Drutis *et al.*, "Three-dimensional chemical imaging of skin using stimulated raman scattering microscopy," *J. Biomed. Opt.*, vol. 19, no. 1, pp. 111604–1-111604-6, May 2014.

[82] M. E. Darvin, C. S. Choe, J. Schleusener, and J. Lademann, "In vivo non-invasive determination of the water concentration and water bonding properties of the human stratum corneum using confocal raman microspectroscopy (mini-review)," *Quantum Electron.*, vol. 51, no. 1, pp. 28–32, 2021.

[83] S. Yakovlev, M. Misra, S. Shi, E. Firlar, and M. Libera, "Quantitative nanoscale water mapping in frozen-hydrated skin by low-loss electron energy-loss spectroscopy," *Ultramicroscopy*, vol. 110, no. 7, pp. 866–876, Jun. 2010.

[84] Z. Haider *et al.*, "Local dosimetry at cellular and subcellular level in HF and millimeter-wave bands," *IEEE J. Microwaves*, vol. 1, no. 4, pp. 1001–1014, Oct. 2021.

ZAIN HAIDER received the M.S. degree in electrical engineering from the National University of Sciences and Technology, Islamabad, Pakistan, in 2017. He is currently working toward the Ph.D. degree in bioelectromagnetics with the Institute of Electronics and Telecommunications of Rennes, University of Rennes 1, Rennes, France. His research interests include microdosimetry and metamaterials.

YVES LE DRÉAN was born in 1964. He received the Ph.D. and Habilitation á Diriger des Recherches degrees in biology from the Université de Rennes 1, Rennes, France, in 1993 and 2007, respectively. In 1994, he joined the Hospital for Sick Children, Toronto, ON, Canada, as a Postdoctoral Fellow. Since 1997, he has been an Associate Professor with the Université de Rennes 1, where he teaches molecular biology and biochemistry. He has authored or coauthored two book chapters, 35 journal publications, and 55 communications in national and international conferences. His main subject of interest is the control of genetic expression. His current research interests include related to the investigations of cell responses to environmental stress. Since 2004, he has been actively involved in the field of biological effects of electromagnetic waves.

GIULIA SACCO (Member, IEEE) received the M.S. degree (*summa cum laude*) in biomedical engineering and the Ph.D. degree (*cum laude* and with the *Doctor Europaeus* label) in information and communication technology from the Sapienza University of Rome, Rome, Italy, in 2017 and 2021, respectively. She is currently a Research Fellow with the Institut d'Électronique et des Technologies du numérique, Rennes, France. From April 2019 to September 2019, she was a Visiting Researcher with Stiching imec Eindhoven, The Netherlands. Her scientific and research interests include innovative biomedical applications of electromagnetic fields and radars for vital signs monitoring.

Dr. Sacco was the recipient of the Best Student Paper Award at Photonics and Electromagnetics Research Symposium (PIERS) 2019 and the Best Student Paper Award at the XXXIII General Assembly and Scientific Symposium (GASS) of the International Union of Radio Science (Union Radio Scientifique Internationale-URSI) 2020.

DENYS NIKOLAYEV (Member, IEEE) received the M.S. degree (*summa cum laude*) in electronics and telecommunications from Lviv Polytechnic National University, Ukraine, in 2008, and the joint Ph.D. degrees in electronics from the Institute of Electronics and Telecommunication of Rennes, Rennes, France, and in electrical engineering from the University of West Bohemia, Pilsen, Czechia, in 2017.

He was a Postdoctoral Fellow with Imec/Ghent University, Belgium, until 2018, a Scientist with École polytechnique fédérale de Lausanne, Lausanne, Switzerland, until 2020, and then joined the French National Center for Scientific Research, Paris, France, as a permanent Researcher. He has authored one book chapter, 20 journal papers, 34 publications in international conference proceedings, and holds four patents. His research interests include wireless bioelectronics and biosensors, antenna theory and design for body-centric networks, bioelectromagnetics, and numerical methods in electromagnetics.

Dr. Nikolayev was the recipient of the Best Ph.D. Dissertation Award by the Foundation Rennes One, the Young Scientist Award at the International Conference EMBEC/NBC 2017, the Best Paper Award at the URSI-France 2017 Workshop, and the Poster Award at BioEM 2015. He was a Laureate of the Eiffel Excellence Doctoral Grant (2015/2016).

RONAN SAULEAU (Fellow, IEEE) graduated in electrical engineering and radio communications from the Institut National des Sciences Appliquées, Rennes, France, in 1995, and received the Agrégation degree from the Ecole Normale Supérieure de Cachan, France, in 1996, and the Doctoral degree in signal processing and telecommunications and the Habilitation á Diriger des Recherches degree from the University of Rennes1, Rennes, France, in 1999 and 2005, respectively.

Between September 2000 and November 2005 and between December 2005 and October 2009, he was an Assistant Professor and Associate Professor with the University of Rennes 1, where he has been a Full Professor since 2009. He has shared the responsibility of the research activities on antennas with IETR, in 2010 and 2011. He was a Co-Director of Research Department Antenna and Microwave Devices, IETR, and the Deputy Director with IETR between 2012 and 2016. He is currently the Director of IETR. He has been involved in more than 60 research projects at the national and European levels and has co-supervised 23 Postdoctoral Fellows, 44 Ph.D. students, and 50 master's students. He has received 17 patents, and is an author or coauthor of more than 250 journal papers and 510 publications in international conferences and workshops. His current research interests include numerical modeling (mainly FDTD), millimeter-wave printed and reconfigurable (MEMS) antennas, substrate integrated waveguide antennas, lens-based focusing devices, periodic and non-periodic structures (electromagnetic bandgap materials, metamaterials, reflectarrays, and transmitarrays), and biological effects of millimeter waves.

Prof. Sauleau was the recipient of the 2004 ISAP Conference Young Researcher Scientist Fellowship, Japan, and the first Young Researcher Prize in Brittany, France, in 2001 for his research work on gain-enhanced Fabry-Perot antennas. In September 2007, he was elevated to a Junior Member of the Institut Universitaire de France. He was awarded the Bronze Medal by CNRS in 2008 and the Silver Medal in 2020. He was the co-recipient of several international conference awards with some of his students (BioEM2005, BEMS'2006, MRRS'2008, E-MRS'2011, BEMS'2011, IMS'2012, Antem'2012, BioEM'2015, and EuCAP'2019). He was the Guest Editor of the IEEE Transactions on Antennas and Propagation Special Issue on Antennas and Propagation at mm and sub mm Waves. He was a National Delegate for several EU COST actions. He was a National Delegate for EurAAP and a Member on the Board of Director of EurAAP from 2013 to 2018.

MAXIM ZHADOBOV (Senior Member, IEEE) received the M.S. degree in electromagnetics from the University of Nizhny Novgorod, Nizhny Novgorod, Russia, in 2003, and the Ph.D. and Habilitation á Diriger des Recherches degrees from the Institut d'Electronique et des Technologies du numerique (IETR), University of Rennes 1, Rennes, France, in 2006 and 2016, respectively.

He was a Postdoctoral Researcher with the Center for Biomedical Physics, Temple University, Philadelphia, PA, USA, until 2008, and then joined the French National Center for Scientific Research (CNRS). He is currently the Principal Investigator of biomedical electromagnetics with the IETR/CNRS and the Head of WAVES Research Team, IETR. He has coauthored five book chapters, five patents, more than 75 research papers in peer-reviewed international journals, and 180 contributions to conferences and workshops. His research interests include innovative biomedical applications of electromagnetic fields and associated technologies. His review article in the *International Journal of Microwave and Wireless Technologies* was the most cited paper in 2016-2020. A paper published by his research group in 2019 is in journal Top 100 of Nature Scientific Reports. He has been involved in 24 research projects (12 as PI).

Dr. Zhadobov was the TPC Co-Chair of BioEM 2021 and BioEM 2020. He was a TPC member and/or session organizer at international conferences, including BioEM 2019, EuMW 2019, IEEE iWEM 2017, MobiHealth 2015-2017, BodyNets 2016, and IMWS-Bio 2014. He is an elected member of EBEA Council, a member of IEEE TC95.4, and the Vice-President of URSI France Commission K. He is an Associate Editor of IEEE Journal of Electromagnetics, RF and Microwaves in Medicine and Biology and was the Guest Editor of several special issues, including the Special Issue on Human Exposure in 5G and 6G Scenarios of Applied Sciences and Advanced Electromagnetic Biosensors for Medical, Environmental and Industrial Applications of Sensors. He was also on review boards of more than 15 international journals and conferences, and has been acting as an expert at research councils worldwide. He was the recipient of the CNRS Medal in 2018, the EBEA Award for Excellence in Bioelectromagnetics in 2015, and Brittany's Young Scientist Award in 2010. Since 2010, his Ph.D. students have been recipients of seven national scientific awards and five awards from the Bioelectromagnetics Society, URSI, and the IEEE Antennas and Propagation Society.